Role of the vessel morphology on the lenticulostriate arteries hemodynamics during atrial fibrillation: A CFD-based multivariate regression analysis

Role of the vessel morphology on the lenticulostriate arteries hemodynamics during atrial fibrillation: A CFD-based multivariate regression analysis

Article *in* Computer Methods and Programs in Biomedicine · June 2024

DOI: 10.1016/j.cmpb.2024.108303

CITATIONS
0

READS
30

8 authors, including:

Andrea Saglietto
Università degli Studi di Torino, Campus Biomedico di Roma
133 PUBLICATIONS **2,419** CITATIONS
SEE PROFILE

Francesco Tripoli
Politecnico di Torino
4 PUBLICATIONS **11** CITATIONS
SEE PROFILE

Geert Jan Biessels
University Medical Center Utrecht
476 PUBLICATIONS **25,237** CITATIONS
SEE PROFILE

Matteo Anselmino
Università degli Studi di Torino
269 PUBLICATIONS **4,908** CITATIONS
SEE PROFILE

Computer Methods and Programs in Biomedicine xxx (xxxx) 108303

Contents lists available at ScienceDirect

Computer Methods and Programs in Biomedicine

journal homepage: www.elsevier.com

Role of the vessel morphology on the lenticulostriate arteries hemodynamics during atrial fibrillation: A CFD-based multivariate regression analysis

Andrea Saglietto [a, b, 1], Francesco Tripoli [c, 1], Jaco Zwanenburg [d], Geert Jan Biessels [e], Gaetano Maria De Ferrari [a, b], Matteo Anselmino [a, b, *], Luca Ridolfi [f], Stefania Scarsoglio [c]

[a] Division of Cardiology, Cardiovascular and Thoracic Department, "Città della Salute e della Scienza" Hospital, Turin, Italy
[b] Department of Medical Sciences, University of Turin, Turin, Italy
[c] Department of Mechanical and Aerospace Engineering, Politecnico di Torino, Turin, Italy
[d] Center for Image Sciences, University Medical Center Utrecht, Utrecht, the Netherlands
[e] UMC Brain Center, University Medical Centre Utrecht, Utrecth, the Netherlands
[f] Department of Environmental, Land and Infrastructure Engineering, Politecnico di Torino, Turin, Italy

ARTICLE INFO

Keywords:
Computational fluid dynamics
Atrial fibrillation
Magnetic resonance imaging
Lenticulostriate arteries
Cerebral circulation
Cognitive decline
Multivariate regression analysis

ABSTRACT

Background and objective: Atrial fibrillation (AF) is the most common cardiac arrhythmia, inducing accelerated and irregular beating. Beside well-known disabling symptoms - such as palpitations, reduced exercise tolerance, and chest discomfort - there is growing evidence that an alteration of deep cerebral hemodynamics due to AF increases the risk of vascular dementia and cognitive impairment, even in the absence of clinical strokes. The alteration of deep cerebral circulation in AF represents one of the least investigated among the possible mechanisms. Lenticulostriate arteries (LSAs) are small perforating arteries mainly departing from the middle cerebral artery (MCA) and susceptible to small vessel disease, which is one of the mechanisms of subcortical vascular dementia development. The purpose of this study is to investigate the impact of different LSAs morphologies on the cerebral hemodynamics during AF.
Methods: By combining a computational fluid dynamics (CFD) analysis of LSAs with 7T high-resolution magnetic resonance imaging (MRI), we performed different CFD-based multivariate regression analyses to detect which geometrical and morphological vessel features mostly affect AF hemodynamics in terms of wall shear stress. We exploited 17 cerebral 7T-MRI derived LSA vascular geometries extracted from 10 subjects and internal carotid artery data from validated 0D cardiovascular-cerebral modeling as inflow conditions.
Results: Our results revealed that few geometrical variables - namely the size of the MCA and the bifurcation angles between MCA and LSA - are able to satisfactorily predict the AF impact. In particular, the present study indicates that LSA morphologies exhibiting markedly obtuse LSA-MCA inlet angles and small MCA size downstream of the LSA-MCA bifurcation may be more prone to vascular damage induced by AF.
Conclusions: The present MRI-based computational study has been able for the first time to: (i) investigate the net impact of LSAs vascular morphologies on cerebral hemodynamics during AF events; (ii) detect which combination of morphological features worsens the hemodynamic response in the presence of AF. Awaiting necessary clinical confirmation, our analysis suggests that the local hemodynamics of LSAs is affected by their geometrical features and some LSA morphologies undergo greater hemodynamic alterations in the presence of AF.

1. Introduction

Atrial fibrillation (AF) is the most common clinical tachyarrhythmia, currently affecting up to 60 million cases worldwide [1]. Due to the progressive rise in life expectancy, and considering that AF typically affects older individuals, this number is definitely expected to grow in the next decades [2]. In recent years, it has been clearly demonstrated that AF is associated to cognitive decline/dementia [3], even in absence

* Corresponding author at: Division of Cardiology, Cardiovascular and Thoracic Department, "Città della Salute e della Scienza" Hospital, Turin, Italy.
E-mail address: matteo.anselmino@unito.it (M. Anselmino).
[1] These authors contributed equally to this work.

https://doi.org/10.1016/j.cmpb.2024.108303
Received 18 April 2024; Received in revised form 11 June 2024; Accepted 23 June 2024
0169-2607/

of clinical cerebrovascular events such as stroke or transient ischemic attacks [4–6]. This association might be promoted by different mechanisms [7–11]: in particular, silent cerebral infarctions, cerebral microbleeds and AF-induced alterations of cerebral blood flow are generally regarded as potentially relevant contributors [12].

Although a partially neglected topic in the past, the study of cerebral hemodynamics during AF has now come into the limelight. Gardarsdottir et al. clearly demonstrated that ongoing AF reduces mean cerebral blood flow compared to sinus rhythm [13]. In addition, the same research group showed that restoring sinus rhythm by elective electrical cardioversion led, in those maintaining sinus rhythm in the following weeks, to a significant improvement in brain perfusion and cerebral blood flow, evaluated by both arterial spin labelling and phase contrast cerebral magnetic resonance imaging (MRI) [14]. Previous research from our group demonstrated that AF not only exerts its hemodynamic effects by lowering mean cerebral perfusion, but also on a beat-to-beat basis. By computational modelling we postulated the occurrence of extreme transient cerebral hemodynamic events (hypoperfusion and hypertensive events) in the deep cerebral circle [15–17] and we subsequently validated these results in vivo using near-infrared spectroscopy (NIRS) [18,19]. Consistently with [14], sinus rhythm restoration by electrical cardioversion eliminated the beat-to-beat hemodynamic effect of AF on the cerebral circle.

Altogether, these recent hemodynamic insights suggest that the silent cerebral lesions unanimously detected in AF patients [8] have, at least partly, a hemodynamic rather than a cardioembolic genesis, as also suggested by their anatomical location (often subcortical) presenting more as the cerebral small vessel disease (SVD) spectrum (lacunar infarctions, white matter lesions and microbleeds) than with typical cardioembolic features [20]. Considering that one of the main vascular supplies to subcortical and white matter areas are the lenticulostriate arteries (LSAs) - small arteries orthogonally departing from anterior (ACA) and middle (MCA) cerebral arteries - we hereby focus on the local cerebral hemodynamics at LSA during AF and normal sinus rhythm (SR).

Computational fluid dynamics (CFD) analyses have recently been exploited to inquire into AF effects on the aortic region [21,22], the formation of thrombi in the left atrial appendage [23,24], as well as stenotic and ischemic stroke conditions on the LSAs [25,26]. By combining the LSAs hemodynamics in AF, in a previously published CFD analysis simulating AF and SR on LSA segmentations derived by 7T high-resolution cerebral magnetic resonance imaging (MRI) [27,28], in AF LSAs resulted to be exposed to an increased range (compared to SR) of wall shear stress (*WSS*), particularly at their origin from the parent cerebral arteries, and to wider ranges of intraluminal pressure along the vessels. Based on these data, AF may affect local hemodynamics at the LSAs level, providing a plausible framework for a direct hemodynamic contribution of AF - on top of other known risk factors (hypertension, diabetes mellitus, smoking, hypercholesterolemia) [29] - in the genesis of non-cardioembolic silent cerebral lesions at the subcortical and white matter level. In fact, it is known that while normal shear stress oscillations are generally athero-protective, excessively low values are pro-atherogenic [30], and extremely high values may induce plaque erosion and rupture [31]. The abovementioned hypervariability in shear stress might therefore imply a higher propensity to activate an atherosclerotic process at the LSA origin, which might facilitate proximal occlusion of the vessel in AF patients. In addition, the increased pressure range to which LSAs are exposed during AF can account for an increased risk of arteriolosclerosis and lipohyalinosis, ultimately facilitating on one side (hypertensive peaks) lacunar strokes or blood–brain barrier damage [29,32] and, on the other side, (hypotensive events) downstream hypoperfusions [15,19].

In the context of such peculiar vessel anatomy - that is the almost perpendicular origin of the small LSAs from relatively large-caliber vessels such as the ACA and MCA - and by recalling that local hemodynamics strongly depends on vascular geometry and that the development of vascular pathologies preferably occurs in regions characterized by a high-complexity geometry, the present study aims at expanding the previous analyses [27,28] by focusing on the role of patient-specific LSA geometrical properties. We hereby evaluated AF-specific local hemodynamic impact on 17 cerebral 7T-MRI derived LSA vascular geometries extracted from 10 subjects, by keeping into account the different geometrical features of each specific geometry, in order to assess which geometrical feature might play a relevant role in exacerbating, or limiting, the beat-to-beat local hemodynamic influence exerted by the irregular AF rhythm. The CFD analysis was performed through Simvascular, an open-source software implementing a finite element method [33,34], which is widely adopted for computationally resolving the 3D fluid dynamics governing equations over MRI-based vascular domains. This approach allowed us to obtain, for each LSA geometry, important hemodynamic parameters related to the *WSS* and flow field in SR and AF conditions.

2. Methods

2.1. MRI data and geometry reconstruction

We exploited cerebral high-resolution 7T MRI data of 10 subjects aged 19 to 75 years (mean age 45 ± 23 years, 50 % males) previously recorded [35]. A 3D T1-weighted magnetization prepared rapid gradient echo sequence was used for the reconstruction of the vasculature geometry, with an acquired resolution of ($0.5 \times 0.5 \times 0.5$ mm^3) and reconstructed resolution of ($0.29 \times 0.29 \times 0.25$ mm^3).

Geometry reconstruction was carried out using the SimVascular MRI-based modeling, as done in [27]. The pipeline includes the identification of each vessel centerline, the 2D segmentation of each vessel lumen, the generation of 3D surfaces fitted to groups of 2D segmentations, and the merging of individual vessels to obtain a full 3D solid model of the vascular district [33,34]. For segmentation purposes, any visible LSA departing either from MCA or ACA on both left and right sides was considered.

Each CFD model was composed of one inlet (MCA or ACA) and two outlets (LSA and MCA or ACA). Flow extensions - consisting of cylindrical segments of the same diameter of the vessel they are applied on - were added to the inlet and the outlets to minimize boundary condition effects and to uniform the length of individual LSAs. In so doing, the distance between the outlet section where pressure condition is set and the LSA-MCA (or LSA-ACA) bifurcation was comparable between the 17 different cases.

2.2. CFD setting: mesh and boundary conditions

3D CFD simulations were run assuming blood as an incompressible, homogeneous and Newtonian fluid, with constant density (ρ = 1060 kg/m^3) and dynamic viscosity (μ = 0.004 kg/(m·s)). All vessels were supposed to be rigid and no-slip condition was set. Under these hypotheses, the blood flow is governed by continuity and Navier-Stokes equations, which were discretized and numerically solved by exploiting the SimVascular simulations tool [27].

The time step size has been set constant equal to 0.05 ms, while the global maximum edge size (GMES) of the unstructured tetrahedral mesh was chosen after a sensitivity analysis on one of the 17 models, selected as representative. Mesh sensitivity analysis was performed considering both three uniform meshes with no boundary layers (with GMES equal 0.017, 0.0135 and 0.0107 cm) and three uniform meshes with the same GMES but three boundary layers, where the density of the mesh in proximity of the vascular wall was increased. The mesh with GMES = 0.017 cm and 3 boundary layers was chosen, being the better compromise between numerical accuracy and affordable computational cost (more details can be found in [28]).

To define the boundary conditions, the workflow shown in Fig. 1 was adopted. The inlet conditions were obtained from the MCA flow rate time series, $Q_{MCA}(t)$, resulting from a combined 0D cardiovascular-cerebral model, which was previously calibrated and validated in SR and AF conditions [15,36].

Through a suitable combination of electrical components, the 0D model accounts for the arterial and venous circuits of both systemic and pulmonary circulations, an active representation of the four cardiac chambers, the cerebral circulation from the large proximal arteries up to the distal and capillary/venous regions, along with the short-term baroregulation and the cerebral autoregulation.

The 0D cardiovascular-cerebral model simulates the cerebral hemodynamics in AF and SR conditions at a heart rate of 70 bpm. To focus on AF impact, we considered each of the 17 models as forced through RR-intervals artificially built in both SR and AF conditions (Fig. 1a) [28,36].

RR beats during SR were extracted from a pink-correlated Gaussian distribution, with mean value $\mu = 0.86$ s. Standard deviation, σ, was determined considering that the coefficient of variation, *cv*, lies in the interval [0.05, 0.14] for SR conditions. Thus, *cv* was kept equal to 0.07 and $\sigma = 0.06$ s [36 and therein references].

The AF beating is fully described by the superposition of two statistically independent times, $RR = \varphi + \eta$, where φ is taken from a Gaussian distribution and the extraction is based on the correlated pink noise, while η is instead drawn from an exponential distribution (with rate parameter γ) and the beating extraction relies on the uncorrelated white noise. The resulting AF beatings are represented by an exponentially modified Gaussian distribution with mean value equal to $\mu = 0.86$ s, as in SR condition. The standard deviation value, σ, is determined keeping the coefficient of variation, *cv*, equal to 0.24. The rate parameter, γ, of the exponential distribution is a linear function of the mean *RR* ($\gamma = -9.2 \cdot RR + 14.6$) [36 and therein references, 37].

5000 beats were run through the 0D cardiovascular-cerebral model in SR and AF (Fig. 1b). Then, for each beat both maximum, Q_{max}, and minimum, Q_{min}, values were collected over the MCA flow rate time series. In this way, two statistically significant sets of 5000 maximum and

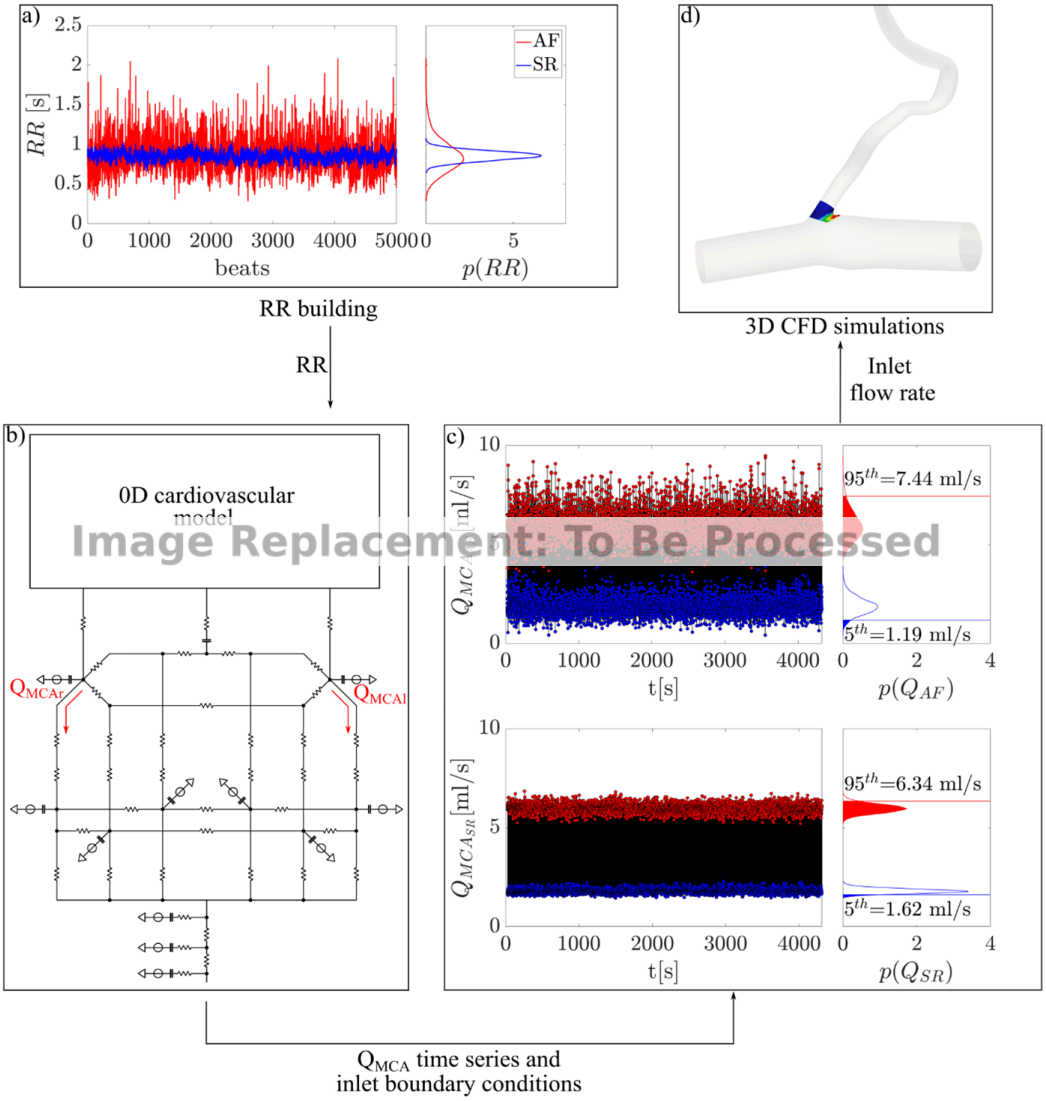

Fig. 1. Schematic representation of the workflow adopted to define the inflow boundary conditions. (a) *RR* series and probability density functions in AF and SR. (b) 0D cardiovascular-cerebral model. (c) $Q_{MCA}(t)$ time series in AF and SR conditions, maximum and minimum values detection, probability density functions $p(Q_{max})$ and $p(Q_{min})$, and computation of the 5th percentile of $p(Q_{min})$ and the 95th percentile of $p(Q_{max})$, both in AF and SR. d) 3D LSA model forced with 4 different inlet flow rates.

minimum values (Q_{max} and Q_{min}, respectively) were sampled. Subsequently, the probability density functions, $p(Q_{max})$ and $p(Q_{min})$, were computed. Then, the 5th percentile of $p(Q_{min})$ and the 95th percentile of $p(Q_{max})$ values were extracted and used as forcing inlets in all vessel models (Fig. 1c). To impose the inlet condition, we computed the Womersley number $Wo = R\sqrt{\omega\rho/\mu}$ ($\omega = 2\pi/RR$, $RR = 0.8571$ s is the cardiac period corresponding to 70 bpm, $\rho = 1060$ kg/m^3, $\mu = 0.004$ kg/(m·s)) for the MCA vessel, which ranges between 1.62 (with the smallest radius, $R = 1.16$ mm) and 2.61 (with the largest radius, $R = 1.87$ mm). As for $Wo < 3$ viscous effects dominate and the profile becomes parabolic as in Poiseuille flow [38], a Poiseuille-like parabolic velocity profile was applied to the entrance. This workflow was performed both in AF and SR conditions at the simulated heart rate of 70 bpm. Therefore, four simulations for each model were simulated: 5th percentile of $p(Q_{min})$ and 95th percentile of $p(Q_{max})$, for both AF and SR conditions (Fig. 1d). Simulations lasting 5000 beats allowed us to capture the complex flow oscillations observed during AF, previously demonstrated to relate to hypoperfusions events in the distal cerebral circle [15], while with the 5th percentile of $p(Q_{min})$ and 95th percentile of $p(Q_{max})$ we focus on the extremely low and high perfusion values, respectively.

To evaluate the main hemodynamic metrics, several regions of interest (ROIs) from the LSA segments were extracted using the Vascular Modeling Toolkit (VMTK). First, the centerlines of the vascular geometry were computed, by tracing weighted shortest paths between two extremal points and bounding them to run on the Voronoi diagram of the vessel model [34]. Secondly, branch splitting was performed based on geometric considerations of the surface, which is fundamental to estimate consistently different morphologies [35]. Finally, branch sections located at a fixed number (n) of maximum inscribed spheres from LSAs origin were computed perpendicularly to the branch centerline.

2.3. Hemodynamic parameter investigated and related statistical analysis

By recalling that all simulations were carried out with constant flow rate inlet conditions, for the purposes of this study *ad hoc* parameters related to *WSS* were introduced to compare SR and AF, and quantify the vascular damage induced by AF. ΔWSS was defined as the difference (in any wall element of each vessel) between the *WSS* magnitude obtained in correspondence of the 95th percentile of $p(Q_{max})$ and that at the 5th percentile of $p(Q_{min})$:

$$\Delta WSS = \left|\overline{WSS_{max}}\right| - \left|\overline{WSS_{min}}\right| \quad (1)$$

where $|*|$ indicates the vector modulus. This metric was computed for SR and AF conditions, obtaining the ΔWSS_{SR} and ΔWSS_{AF} maps for each model. ΔWSS is a local metric quantifying the excursion that *WSS* undergoes when the vascular region is stressed by hyper-perfusion (95th percentile of $p(Q_{max})$) and hypoperfusion (5th percentile of $p(Q_{min})$) conditions. To investigate this metric a ROI with $n = 2$ (n is the number of inscribed spheres) was considered, according to the sensitivity analysis reported in [28].

Statistical analysis involved different multivariate regressions between different geometric descriptors of vessels (predictor variables) and the 90th percentile value of the spatial distribution of the wall shear stress difference,

$$WSSd = \Delta WSS_{AF} - \Delta WSS_{SR}, \quad (2)$$

as response variable. *WSSd* describes (in any point of the vessel wall) the *WSS* jump between maximum and minimum flow rates in AF and SR. Since in general $\Delta WSS_{AF} > \Delta WSS_{SR}$, *WSSd* is a metric assuming positive values throughout the spatial domain and reveals the different stress induced by AF with respect to SR. Taking the 90th percentile of *WSSd* ($WSSd_{90}$) means focusing, for each model, on the vascular regions mostly impacted by AF (Fig. 2).

A set of vessel-specific geometric features was extracted by exploiting the VMTK software, which allowed a robust geometric characterization based on centerlines computation and geometric considerations [39,40]. This analysis led to a total of 11 geometric variables: four variables related to bifurcation angles, six variables related to the inlet, outlet and LSA radii, and one variable related to the LSA tortuosity (Table 1). More specifically, these variables are (Fig. 3):

- inlet-LSA in-plane bifurcation angle: angle between the in-plane components of the inlet and LSA bifurcation vectors;
- outlet-LSA in-plane bifurcation angle: angle between the in-plane components of the outlet and LSA bifurcation vectors;
- inlet-LSA out-of-plane bifurcation angle: angle between the out-of-plane components of the inlet and LSA bifurcation vectors;
- outlet-LSA out-of-plane bifurcation angle: angle between the out-of-plane components of the outlet and LSA bifurcation vectors;
- maximum inscribed sphere radius computed on the origin points A, B and C of each centerline tract;
- mean of the maximum inscribed spheres radii computed, for each tract, from the centerline origin point (A, B or C) to the centerline point on the last branch section of interest (ROI 1 for inlet and outlet, ROI 2 for LSA);
- LSA tortuosity computed as:

$$\frac{L}{D} - 1$$

where L is the length of the centerline from the origin to the point on the ROI 2 branch section, and D is the Euclidean distance between the same points.

Both geometric and predictor variables were evaluated at the proximal portion of the LSAs, by defining appropriate ROIs based on the vessel size. In particular, branch sections located at a fixed number (n) of maximum inscribed spheres from LSAs origin were computed perpendicularly to the branch centerline. Here, $n = 1$ (Inlet and Outlet, ROI 1) and $n = 2$ (LSA, ROI 2) maximum inscribed spheres away from the bifurcation were selected (Fig. 3) [28].

Firstly, the linear correlation coefficient r_{ij} between each pair of columns in Table 1 was computed, resulting in a correlation matrix R_{ij} reported in Table 2. Secondly, to determine which geometric variables were most relevant, the following workflow was used: initially, the regressions between a single predictor variable and the response variable were computed, and, among all the predictors, the one that allowed to obtain the regression with the highest R^2 coefficient was selected. Subsequently, the regressions were implemented using two predictor variables, where the first one corresponds to the variable chosen in the previous step.

The variables that allowed to obtain the highest R^2 were selected. This workflow was followed in order to perform all possible multivariate regressions, and, for each step, the best variables combination was chosen.

Two different models were used to compute regressions. The first one is linear:

$$y = \alpha_0 + a_1 \cdot x_1 + \ldots + a_n \cdot x_n \quad (3)$$

where y and x_i are the response and predictor variables, respectively. The second one is a non-linear model according to the following expression:

$$y = \beta_0 \cdot x_1^{\beta_1} \cdot x_2^{\beta_2} \cdot \ldots \cdot x_n^{\beta_n} \quad (4)$$

In this latter case, by performing a logarithmic transformation, the problem returns linear.

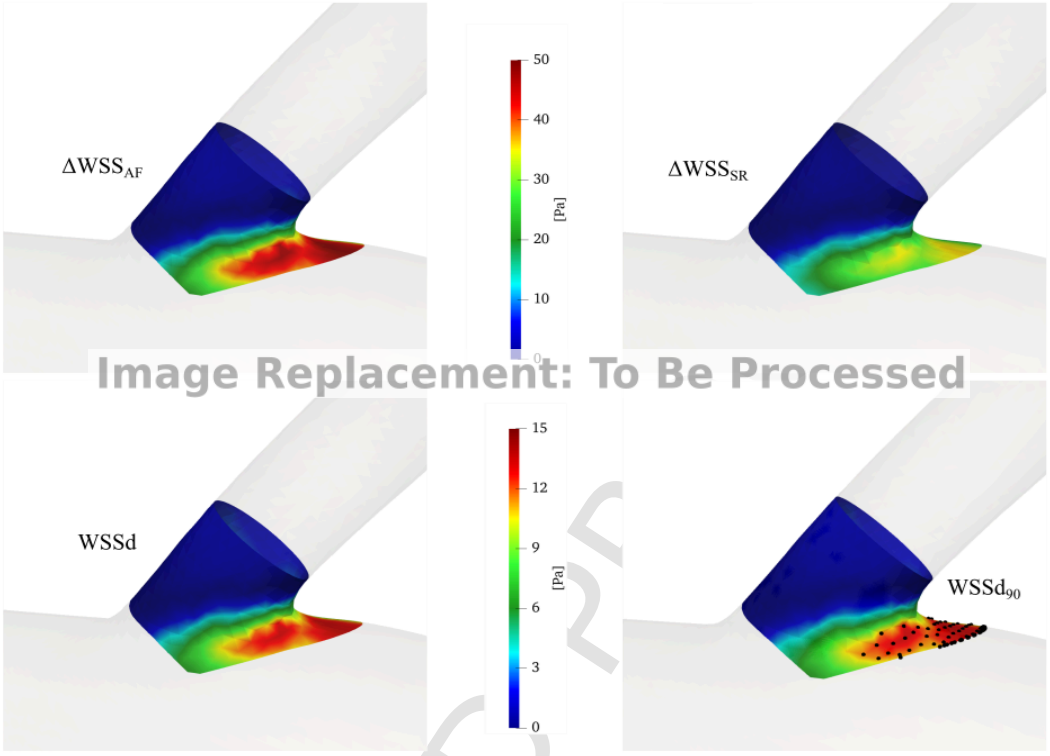

Fig. 2. CFD models of a representative LSA (patient V2043) displaying local Δ*WSS* values (top panels, AF left and SR right) and *WSSd* spatial distribution (bottom left panel). In the right bottom panel black points show where the *WSSd* is greater than $WSSd_{90}$.

Table 1
Geometric (first 11 columns) and response (last column) variables evaluated for the 17 LSAs models analyzed (rows).

In Plane Angle LSA-Inlet (°)	Out Plane Angle LSA-Inlet (°)	In Plane Angle LSA-Outlet (°)	Out Plane Angle LSA-Outlet (°)	Radius inlet ROI1 (mm)	Mean radius inlet ROI1 (mm)	Radius outlet ROI1 (mm)	Mean radius outlet ROI1 (mm)	Tortuosity LSA ROI2	Radius LSA (mm)	Mean radius LSA ROI2 (mm)	$WSSd_{90}$ (Pa)
80.73	6.18	108.50	1.29	1.35	1.33	1.36	1.36	0.060	0.50	0.48	1.84
88.48	36.68	108.36	39.29	1.44	1.45	1.39	1.38	0.111	0.61	0.54	3.16
102.15	12.30	103.40	4.94	1.37	1.37	1.33	1.32	0.012	0.44	0.53	6.55
114.62	10.35	71.82	7.16	1.31	1.32	1.35	1.35	0.014	0.44	0.38	2.85
82.76	10.42	109.86	13.49	1.50	1.49	1.52	1.52	0.010	0.39	0.37	1.62
76.97	3.13	116.78	2.30	1.51	1.51	1.52	1.52	0.029	0.42	0.40	1.64
69.16	16.45	109.67	13.30	1.52	1.52	1.47	1.44	0.070	0.43	0.42	2.80
65.84	6.33	124.17	7.11	1.44	1.41	1.47	1.46	0.067	0.44	0.45	0.83
131.95	4.32	69.53	12.94	1.49	1.49	1.47	1.43	0.017	0.48	0.42	3.81
98.31	6.78	103.52	6.74	1.46	1.46	1.48	1.48	0.009	0.53	0.48	2.95
70.64	9.51	125.26	1.65	1.37	1.35	1.44	1.46	0.116	0.47	0.45	2.91
124.28	2.85	77.19	10.00	1.16	1.15	1.19	1.17	0.010	0.45	0.40	11.03
108.10	20.08	83.75	26.11	1.50	1.49	1.51	1.52	0.065	0.62	0.54	1.83
73.98	3.85	112.01	2.74	1.50	1.47	1.47	1.48	0.132	0.36	0.38	1.53
108.32	10.41	93.10	7.57	1.87	1.86	1.86	1.83	0.018	0.47	0.44	1.41
84.34	11.61	101.26	16.92	1.72	1.72	1.68	1.66	0.010	0.51	0.45	1.55
93.00	0.57	103.00	5.64	1.54	1.59	1.58	1.57	0.084	0.37	0.43	1.74

3. Results

Fig. 4 shows the highest R^2 values as function of the predictor variable that at each step was added to those of the previous step, with three different multivariate regression models: linear regression (panel (a)), non-linear regression considering logarithmic-transformed variables (panel (b)), and non-linear regression in the space of the original (non-transformed) variables (panel (c)). With all the models, the coefficient R^2 increases (in one case non-monotonically) with the number of predictors used for the regression.

The multivariate linear regression in Fig. 4a shows that the first four predictors - i.e., r outlet mean, in plane angle LSA-inlet, in plane angle LSA-outlet, r outlet 1 - are sufficient to reach a value of R^2 above 0.75. Fig. 4b displays the highest R^2 coefficients computed in the logarithms space of the starting variables obtained at each step from the multivariate non-linear regressions. Contrary to the previous case, where an asymptotic value of 0.8 was reached with the first four predictors, R^2 continues to increase plateauing to a value of approximately 0.9 after the first nine predictors. In the end, Fig. 4c shows the highest R^2 coefficients computed in the origin space of the starting variables obtained at each step from the multivariate non-linear regressions.

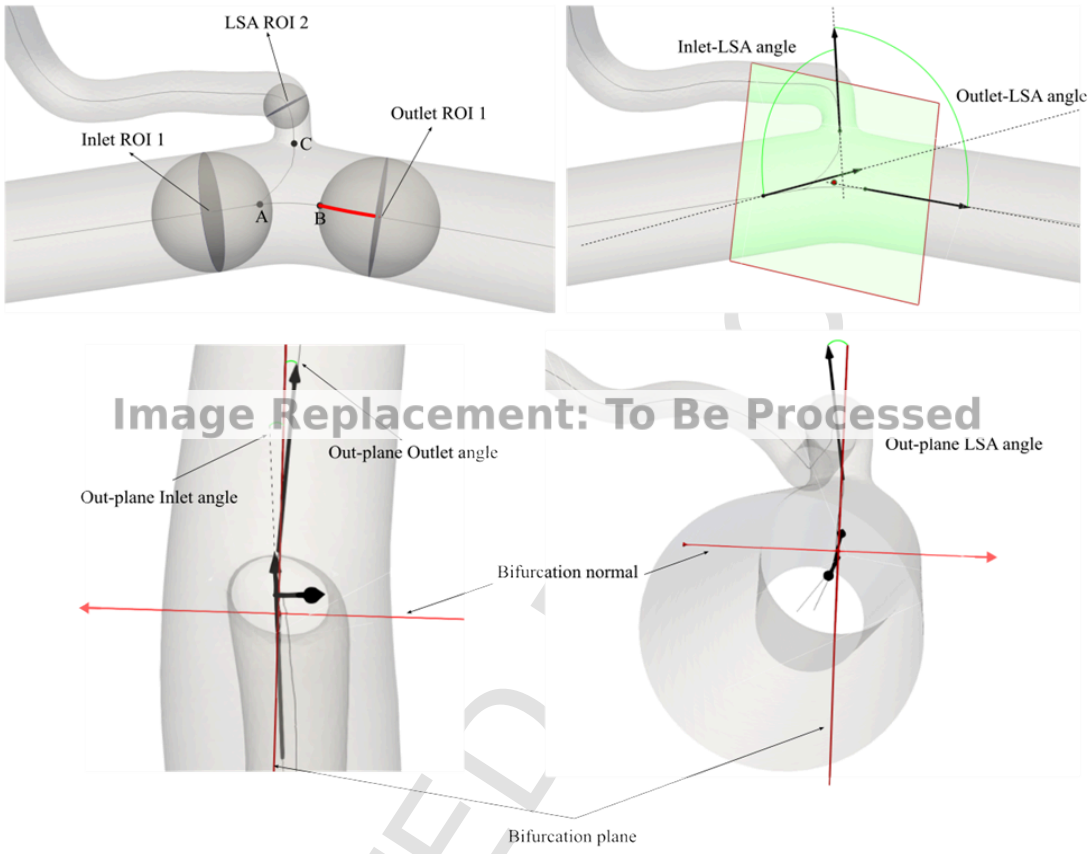

Fig. 3. Vessel-specific geometric features. Top left panel: branch sections located at one (Inlet and Outlet) and two (LSA) maximum inscribed spheres away from the bifurcation. A, B and C are the closest points to the bifurcation region which belong to the centerline tracts (Inlet, Outlet, LSA) obtained after branch decomposition. Top right panel: bifurcation vectors (black), bifurcation plane (green) and bifurcation angles. Bottom panels: out-of-plane components of the outlet and inlet (left), and LSA (right) bifurcation vectors. The out-of-plane bifurcation angles shown in Table 1 can be obtained by computing the difference between these components.

Compared to the previous results, R^2 assumes higher values and, with the first four predictors - r outlet mean, in plane angle LSA-inlet, in plane angle LSA-outlet, r inlet mean - values around 0.9 are reached. In all the three cases analyzed the first three predictors, providing a R^2 value of at least 0.75 which satisfactorily describes the response variable ($WSSd_{90}$), are identical and in the same order of statistical relevance: the MCA (or ACA) outlet mean radius within ROI 1 (r outlet mean), the in-plane bifurcation angle between the LSA and the MCA (or ACA) inlet (in plane angle LSA-inlet), and the in-plane bifurcation angle between the LSA and the MCA (or ACA) outlet (in plane angle LSA-outlet). This result confirms the high level of hemodynamic information that these 3 geometric parameters, uncorrelated one from each other (see Table 2) and independently of the chosen regression model, are able to yield.

To further investigate the role of the three most informative variables, Fig. 5 displays the scatter plots between the actual response variable (x-axis) versus the predicted (y-axis) values estimated by a multivariate linear (panel a) and non-linear (panel b) regression model using the first 3 predictors. In fact, after conducting the multivariate regressions and estimating the α and β coefficients, relative to Eqs. (3) and (4), respectively, it is possible to determine the $WSSd_{90}$ predicted values. For both linear and non-linear regression models, the predictors x_1, x_2, and x_3 are the variables r outlet mean, in plane angle LSA-inlet, and in plane angle LSA-outlet, respectively.

Both models provide good prediction of $WSSd_{90}$, however the linear model yields an R^2 of 0.72, while a non-linear model yields an R^2 of 0.89. As a result, the scatter plot markers displayed in Fig. 5b are closer to the red bisector line, which represents the ideal prediction ($R^2 = 1$).

Fig. 6 shows two representative cases where the *WSSd* maps reach the highest (top panel) and lowest (bottom panel) values (*WSSd* maps of the other 15 models not shown here are reported in the Supplementary Material, see Fig. S1). In both cases, the highest values within the LSA ROI 2 are reached at the junction between the LSA wall and the upper wall of the MCA outlet: the 90th percentile is 11.03 Pa for the top panel, while 0.83 Pa for the bottom panel. The two displayed configurations with the most extreme *WSSd* values allow us to inquire into the role of the three most important morpho-geometric predictors in determining the *WSSd* magnitude. In fact, the model with the highest *WSSd* value (top panel) shows a morphological configuration with the lowest r outlet mean value (1.17 mm), one of the highest in plane LSA-inlet angles (124.28°, well above 90°), and one of the lowest in plane LSA-outlet angles (77.19°, lower than 90°). On the contrary, the model with the lowest *WSSd* value (bottom panel) exhibits an intermediate r outlet mean value (1.46 mm) with respect to the other models, the lowest in plane LSA-inlet angle (65.84°, much lower than 90°), and one of the highest in plane LSA-outlet angles (124.17°, much higher than 90°). Note that the two configurations display in plane LSA-inlet and LSA-outlet angles which are inverted with respect to each other: the highest *WSSd* occurs with an obtuse (acute) in plane LSA-inlet angle (in plane LSA-outlet angle), while the lowest *WSSd* emerges with an acute (obtuse) in plane LSA-inlet angle (in plane LSA-outlet angle).

Table 2
Correlation matrix R_{ij}. Linear correlation coefficient values computed between each pair of columns in Table 1: red: $|r_{ij}|<0.25$; orange: $0.25 \leq |r_{ij}|<0.5$; yellow: $0.5 \leq |r_{ij}|<0.75$; green: $0.75 \leq |r_{ij}|<1$.

	In Plane Angle LSA-Inlet	Out Plane Angle LSA-Inlet	In Plane Angle LSA-Outlet	Out Plane Angle LSA-Outlet	Radius inlet ROI1	Mean radius inlet ROI1	Radius outlet ROI1	Mean radius outlet ROI1	Tortuosity LSA ROI2	Radius LSA	Mean radius LSA ROI2	$WSSd_{90}$
In Plane Angle LSA-Inlet	1.00	−0.07	−0.93	0.17	−0.13	−0.12	−0.15	−0.18	−0.55	0.24	−0.01	0.54
Out Plane Angle LSA-Inlet		1.00	0.04	0.86	0.08	0.07	−0.03	−0.03	0.27	0.69	0.64	−0.068
In Plane Angle LSA-Outlet			1.00	−0.21	0.11	0.10	0.14	0.18	0.51	−0.22	0.07	−0.43
Out Plane Angle LSA-Outlet				1.00	0.12	0.12	0.01	−0.01	0.12	0.70	0.59	0.01
Radius inlet ROI1					1.00	0.99	0.97	0.96	−0.07	0.02	0.10	−0.63
Mean radius inlet ROI1						1.00	0.97	0.95	−0.05	−0.01	0.08	−0.61
Radius outlet ROI1							1.00	0.99	−0.07	−0.03	0.05	−0.67
Mean radius outlet ROI1								1.00	−0.03	−0.02	0.07	−0.70
Tortuosity LSA ROI2									1.00	0.01	0.29	−0.31
Radius LSA										1.00	0.90	0.01
Mean radius LSA ROI2											1.00	−0.14
$WSSd_{90}$												1.00

Fig. 7 depicts, for the same cases of Fig. 6 (top panels model yielding to the highest *WSSd*, bottom panels model with the lowest *WSSd*), zoomed flow field streamlines obtained considering a flow rate equal to the 95th percentile of $p(Q_{max})$ (left panels) and to the 5th percentile of $p(Q_{min})$ (right panels). These two flow rates are representative of flow fields exhibiting the highest and the lowest velocity magnitudes considered in the present study. We only consider the AF case (SR not shown here), as the AF rhythm gives rise to the highest values of the 95th percentile of $p(Q_{max})$ and the lowest values of the 5th percentile of $p(Q_{min})$ (that is, 95th percentile of $p(Q_{max,AF})$ > 95th percentile of $p(Q_{max,SR})$ and 5th percentile of $p(Q_{min,AF})$ < 5th percentile of $p(Q_{min,SR})$).

Considering that the two flow rate values (7.44 ml/s and 1.19 ml/s) are the same for both cases, the resulting differences in terms of velocity field are only due to the different geometrical and morphological features. Top panels of Fig. 7 show higher velocity values than the corresponding bottom panels due to the fact that the model with the highest *WSSd* value (top panels) has the lowest *r* outlet mean value. Since *WSS* and velocity field are correlated, in the top panels configuration both the velocity magnitude and *WSS* are higher in AF than SR for the Q_{max} case, while both lower in AF than SR for Q_{min}. Instead, bottom panels are related to the lowest *WSSd* reached, thus the velocity field and *WSS* are quite similar (either for $p(Q_{max})$ or $p(Q_{min})$) in AF and SR.

Recirculating and flow separation regions are present close to the LSA inlet. In the top panels, these regions are visible for both Q_{max} and Q_{min}. In the Q_{max} case (top left), due to the higher velocity, this region is partially advected downstream along the MCA, giving rise to disturbed, separated, and not parallel streamlines (these aspects are further amplified by the slight MCA curvature nearby the LSA inlet). In the Q_{min} case (top right), the recirculating region is smaller in size and basically attached to the LSA inlet. Here, the flow slows down (slower in AF than in SR), enhancing blood stagnation. In the bottom panels, recirculation is present only for Q_{max} (bottom left), while is absent for Q_{min} (bottom right). Apart from the LSA region, these Q_{max} and Q_{min} configurations both induce parallel and poorly disturbed streamlines without flow separation, and similar velocity magnitudes in SR and AF.

4. Discussion

The results presented show that few morpho-geometric predictor variables - namely the MCA outlet mean radius within ROI 1, the in-plane bifurcation angle between the LSA and the MCA inlet, and the in-plane bifurcation angle between the LSA and the MCA outlet - are able to accurately describe ($R^2>0.75$ and $R^2>0.85$ according to the linear and nonlinear regression, respectively) the AF impact in terms of *WSS*, through the *WSSd* metric as response variable. The predictor variables detection and order of appearance is quite robust, as it is the same for the three models tested (linear regression, non-linear regression with logarithmic variables, non-linear regression with origin variables). By analyzing the sign of coefficients of first three regressors, for all the models tested it emerged that an increase of the MCA outlet mean radius within ROI 1 reduces the *WSSd* metric, while augmenting in-plane inlet and outlet bifurcation LSA-MCA angles leads to an increase of the *WSSd* metric.

The analysis of cases yielding the highest and the lowest *WSSd* values evidences which vascular morphology is more and less prone to the AF impact, respectively. The lowest *WSSd* case is caused by an intermediate r outlet mean value, an acute in plane LSA-inlet angle, and an obtuse in plane LSA-outlet angle. This is the configuration where velocity field and *WSS* distributions are comparable in AF and SR, thus preferable as the AF impact is minimized.

On the contrary, the highest *WSSd* is due to a small r outlet mean value (which implies higher *WSS* and velocity values, as observed in top panels of Figs. 6 and 7), an obtuse in plane LSA-inlet angle, and an acute in plane LSA-outlet angle. By recalling that the *WSSd* metric is defined as:

Image

it can be reformulated as follows:

$$WSSd = \left(\left|\overrightarrow{WSS_{max,AF}}\right| - \left|\overrightarrow{WSS_{max,SR}}\right|\right) - \left(\left|\overrightarrow{WSS_{min,AF}}\right| - \left|\overrightarrow{WSS_{min,SR}}\right|\right)$$

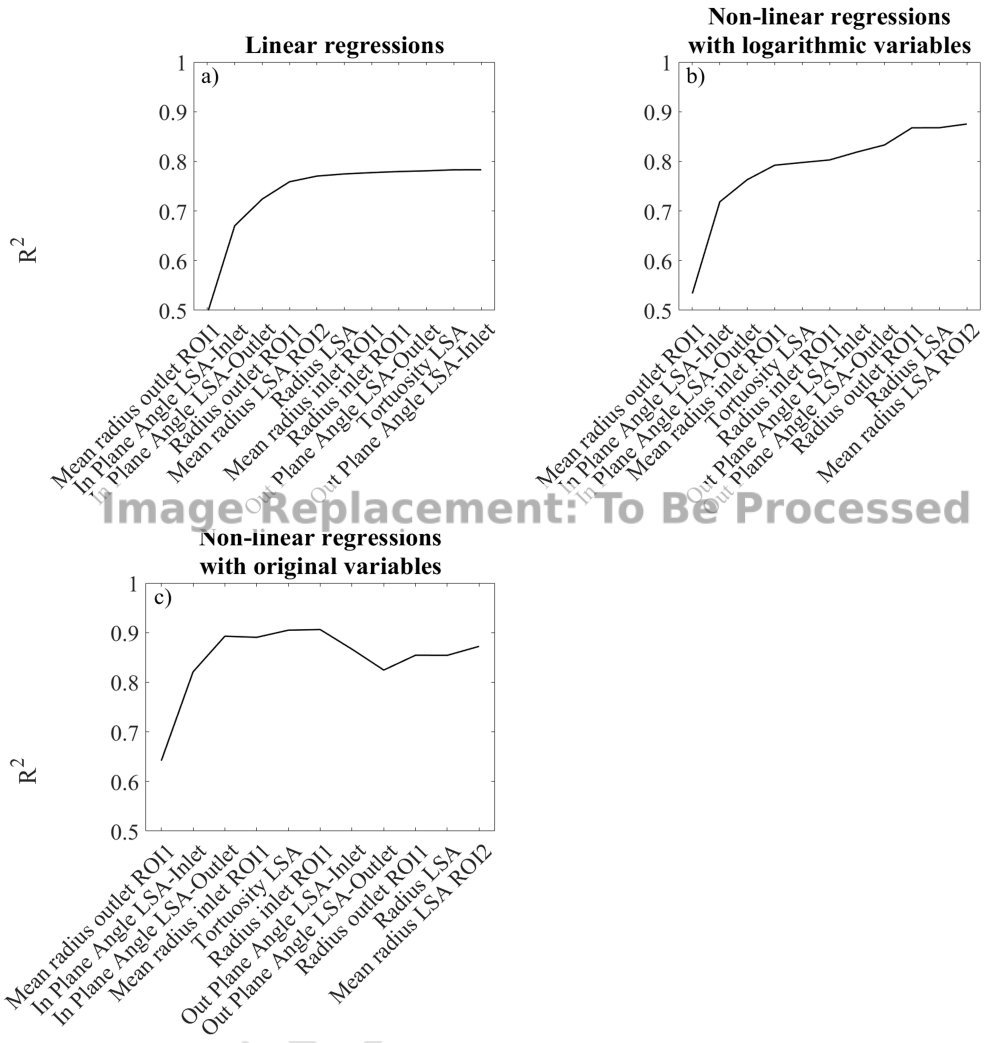

Fig. 4. (a) R^2 coefficient values in relation to the number of predictors used for linear regression. (b) R^2 coefficient values in relation to the number of predictors used for non-linear regression with logarithmic-transformed variables. (c) R^2 coefficient values in relation to the number of predictors used for non-linear regression with original (non-transformed) variables.

where we observe that WSSd can be maximize either because $WSS_{max,AF} \gg WSS_{max,SR}$ (for Q_{max} flow rate) or $WSS_{min,AF} \ll WSS_{min,SR}$ (for Q_{min} flow rate).

In order to understand the influence of the two terms $\left(\left|\overrightarrow{WSS_{max,AF}}\right| - \left|\overrightarrow{WSS_{max,SR}}\right|\right)$ and $\left(\left|\overrightarrow{WSS_{min,AF}}\right| - \left|\overrightarrow{WSS_{min,SR}}\right|\right)$, Fig. 8 reports them for the highest (top panels) and lowest (bottom panels) *WSSd* values reached (same cases as displayed in Figs. 6 and 7). With respect to the lowest *WSSd*, for the highest *WSSd* case the contribute of both terms $\left(\left|\overrightarrow{WSS_{max,AF}}\right| - \left|\overrightarrow{WSS_{max,SR}}\right|\right)$ and $\left(\left|\overrightarrow{WSS_{min,AF}}\right| - \left|\overrightarrow{WSS_{min,SR}}\right|\right)$ is relevant. In fact, top panels of Fig. 8 show that the LSA inlet close to the superior MCA wall experiences, on one hand, very high *WSS* values in AF (top left panel, Q_{max} flow rate), inducing important mechanical stress at the wall and, potentially, hypertensive events [41,42]. On the other hand, when Q_{min} flow rate is considered (top right panel), the same region (LSA inlet close to the superior MCA wall) is exposed to very low *WSS* in AF, thus the flow slows down and recirculates (as also confirmed by the streamlines in Fig. 7 top right), increasing the atheroprone risk [43,44]. In the lowest *WSSd* model (Fig. 8, bottom panels), all the *WSS* differences between AF and SR are definitely reduced and thus the risks of high mechanical stress and atherogenesis minimized.

Finally, it is interesting to note that the models inducing the highest and the lowest *WSSd* values do not have in plane LSA-inlet and in plane LSA-outlet angles close to the orthogonal value, that is, in the range [70°, 110°]. The LSAs are known to be commonly perpendicular to the parent MCA/ACA [45], which is also found in our dataset: from Table 1, 12 models (out of 17) have in plane LSA-inlet and in plane LSA-outlet angles in the range [70°, 110°]. However, deviation from this more common morphology is possible and these less frequent geometrical features concur, together with the size of the originating MCA/ACA vessel, to exacerbate (obtuse in plane LSA-inlet angle) or damp (acute in plane LSA-inlet angle) the AF effect. Deviation from the common morphology can also be due to vascular abnormalities such as stenosis or aneurysms, which can primarily affect the lumen size, by enlarging (aneurysms) or reducing (stenosis) it, and to a lesser extent also the MCA-LSA bifurcation angles. We expect that including these morphologies would lead to more extreme values of the first significant regressors, that is vessel size and bifurcations angles, thus increasing the variability of the sample in the regression analysis. In this regard, the significancy of the first regressors is expected to be strengthened and maintained in the same order.

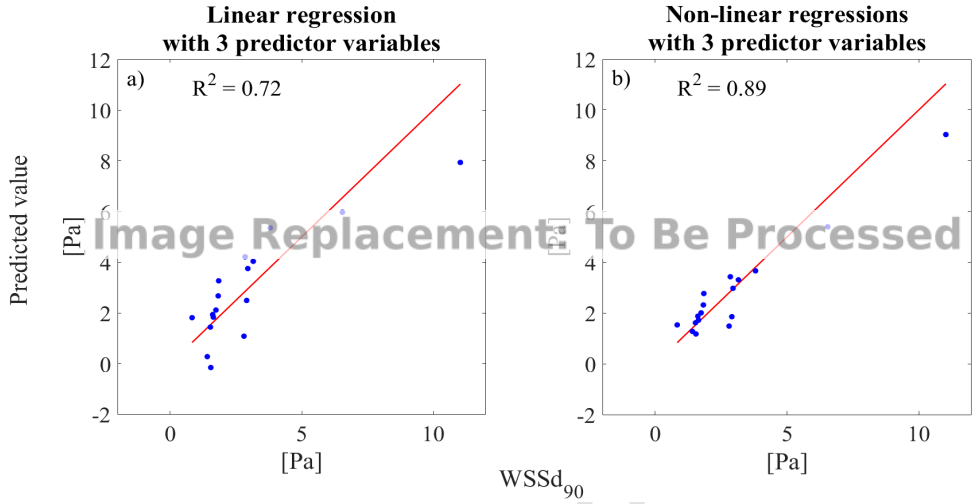

Fig. 5. (a) Scatter plot of Actual vs. Predicted values of the $WSSd_{90}$ difference obtained from the linear regression computed using the three most informative regressors. (b) Scatter plot of Actual vs. Predicted $WSSd_{90}$ obtained from the non-linear regression computed using the three most informative regressors.

We acknowledge that the current study presents some limiting aspects, mostly related to computational fluid dynamic analyses carried out. First, rigid wall assumption was considered, neglecting deformation and compliant effects of the distal cerebral circulation, although the low compliance of cerebral vessels and their low pulse pressure should attenuate the effects of vessel deformability. Second, in order to force all the models with the same flow rate, MCA flow rate was assumed as inlet condition for all the 17 vascular geometries, including the 3 models departing from ACA. In the end, a database with a greater number of models could further consolidate the proposed statistical analysis. We acknowledge that 17 models represent a small sample. However, even with this small set, we already appreciate a significant variability of the morphology and the values reached by the response variables as well as by the most meaningful regressors. Present findings can be generalized and extended to a broader range of cases. We expect that a higher number of models can modify the weight of each regressor and thus improve the robustness of the predictive models proposed. At the same time, given the high level of information achieved by the first most significant regressors even with a small sample, we expect the same predictor variables with the same order of significance to be identified.

5. Conclusions

In conclusion, the present MRI-based computational study has been able for the first time to: (i) investigate the net impact of LSAs vascular morphologies on cerebral hemodynamics during AF events; (ii) detect, among the analyzed models, which combination of morphological features worsens the hemodynamic response in the presence of AF. Awaiting necessary clinical confirmation and a larger sample of MRI data, our analysis suggests that the local hemodynamics of LSAs is affected by their geometrical features and some LSA morphologies undergo greater hemodynamic alterations in the presence of AF. In particular, LSA morphologies exhibiting markedly obtuse in plane LSA-MCA inlet angles and small MCA radii downstream of the LSA-MCA bifurcation may be more prone to vascular damage induced by AF.

CRediT authorship contribution statement

Andrea Saglietto: Writing – review & editing, Writing – original draft, Supervision, Conceptualization. **Francesco Tripoli:** Writing – review & editing, Writing – original draft, Visualization, Software, Methodology, Formal analysis. **Jaco Zwanenburg:** Writing – review & editing, Resources. **Geert Jan Biessels:** Writing – review & editing, Resources. **Gaetano Maria De Ferrari:** Writing – review & editing, Conceptualization. **Matteo Anselmino:** Writing – review & editing, Supervision, Conceptualization. **Luca Ridolfi:** Writing – review & editing, Supervision, Methodology, Formal analysis, Conceptualization. **Stefania Scarsoglio:** Writing – review & editing, Writing – original draft, Supervision, Methodology, Funding acquisition, Formal analysis, Conceptualization.

Declaration of competing interest

The authors declare that they have no known competing financial interests or personal relationships that could have appeared to influence the work reported in this paper.

Acknowledgments

This study was carried out within the 2022EAN2BB "Cerebral fluid dynamics: investigating the association between atrial fibrillation and dementia through an integrated in silico-in vivo framework" project – funded by the Ministero dell'Università e della Ricerca – within the PRIN 2022 program (D.D.104 - 02/02/2022). This manuscript reflects only the authors' views and opinions and the Ministry cannot be considered responsible for them.

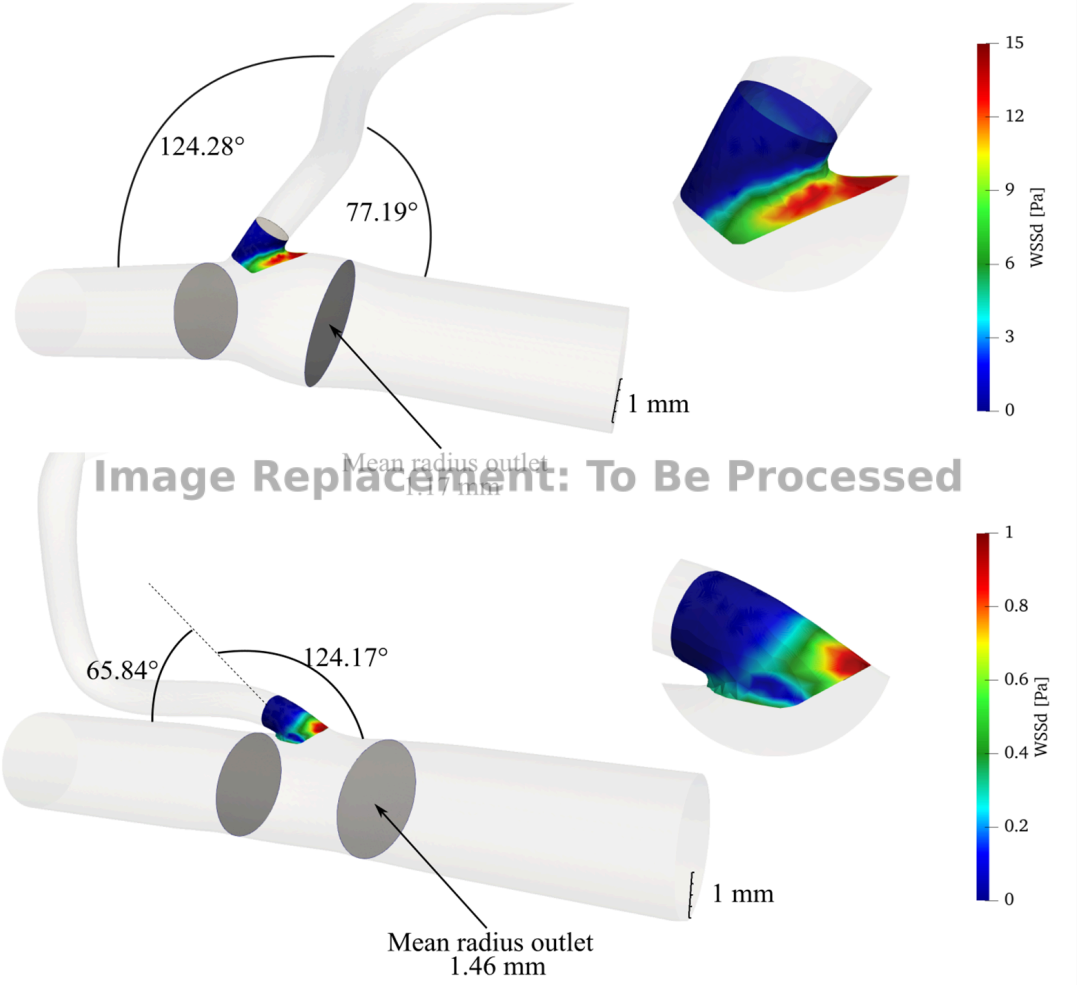

Fig. 6. *WSSd* maps for the models reaching the highest (top panel) and the lowest (bottom panel) *WSSd* values (length scale reported is 0.1 cm for both panels).

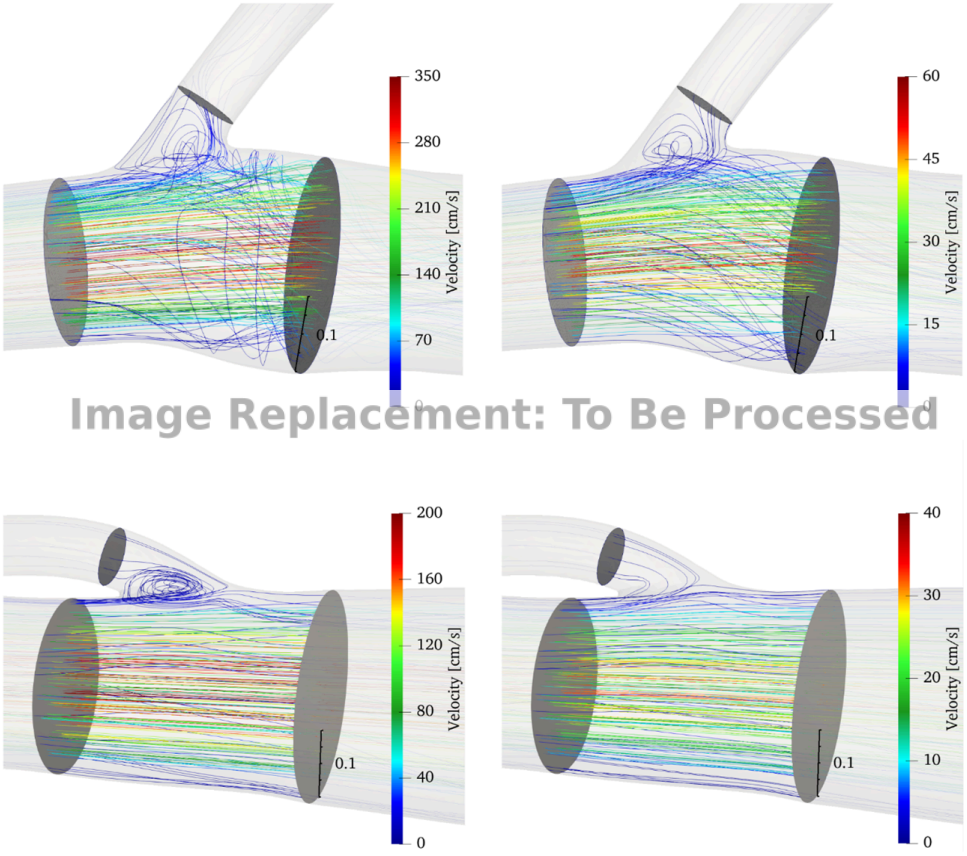

Fig. 7. Streamlines of the models exhibiting the highest (top panels) and the lowest (bottom panels) *WSSd* in AF. The resulting flow field is obtained for a flow rate equal to the 95th percentile of $p(Q_{max})$ (left panels) and to the 5th percentile of $p(Q_{min})$ (right panels).

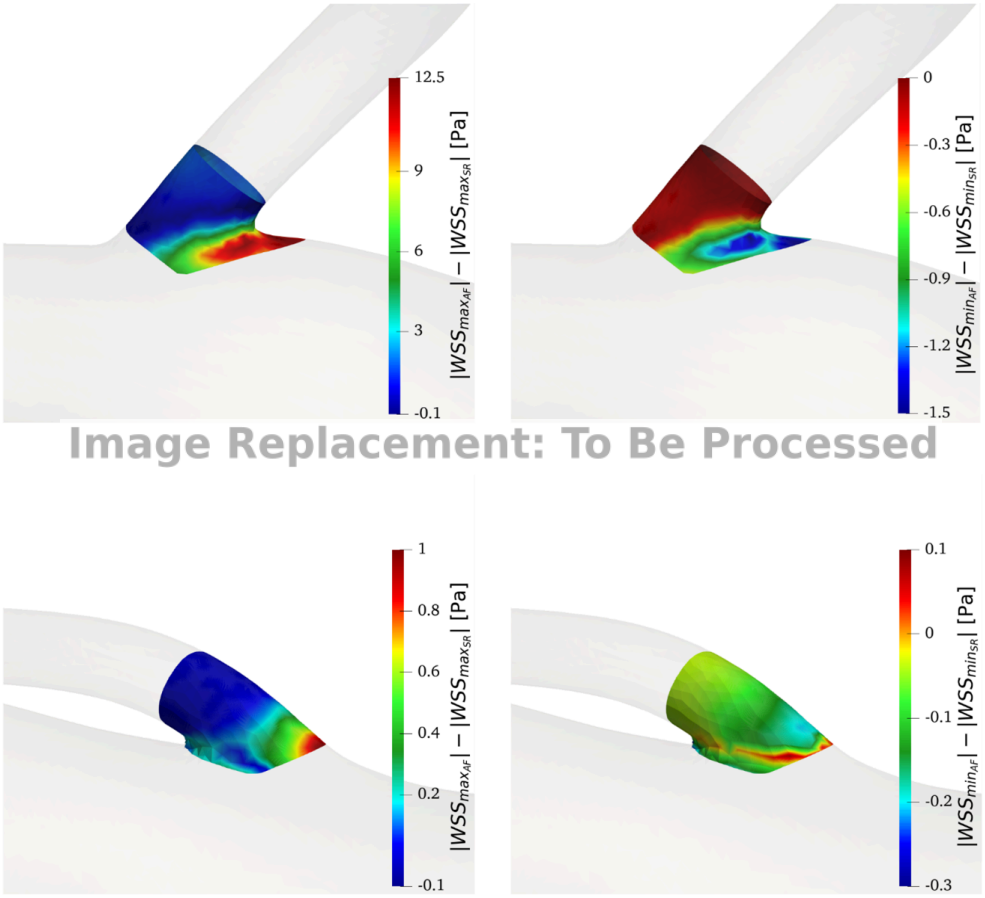

Fig. 8. Maps of differences $\left(\left|\overline{WSS_{max,AF}}\right| - \left|\overline{WSS_{max,SR}}\right|\right)$ and $\left(\left|\overline{WSS_{min,AF}}\right| - \left|\overline{WSS_{min,SR}}\right|\right)$ on the left (Q_{max}) and right (Q_{min}) panels, respectively, for the models exhibiting the highest (top panels) and the lowest (bottom panels) *WSSd* in AF.

Supplementary materials

Supplementary material associated with this article can be found, in the online version, at doi:10.1016/j.cmpb.2024.108303.

References

[1] G.A. Roth, G.A. Mensah, C.O. Johnson, G. Addolorato, E. Ammirati, L.M. Baddour, et al., Global burden of cardiovascular diseases and risk factors, 1990–2019: update from the GBD 2019 study, J. Am. Coll. Cardiol. 76 (25) (2020) 2982–3021.

[2] G. Hindricks, T. Potpara, N. Dagres, E. Arbelo, J.J. Bax, C. Blomstrom-Lundqvist, et al., 2020 ESC guidelines for the diagnosis and management of atrial fibrillation developed in collaboration with the European Association for Cardio-Thoracic Surgery (EACTS), Eur. Heart J. 42 (5) (2021) 373–498.

[3] A. Saglietto, A. Ballatore, H. Xhakupi, G.M. De Ferrari, M. Anselmino, Atrial fibrillation and dementia: epidemiological insights on an undervalued association, Medicina (Kaunas) 58 (3) (2022) 361.

[4] V. Jacobs, M.J. Cutler, J.D. Day, T.J. Bunch, Atrial fibrillation and dementia, Trends Cardiovasc. Med. 25 (1) (2015) 44–51.

[5] S. Hui, J.E. Morley, P.C. Mikolajczak, R. Lee, Atrial fibrillation: a major risk factor for cognitive decline, Am. Heart J. 169 (4) (2015) 448–456.

[6] A. Saglietto, M. Matta, F. Gaita, V. Jacobs, T.J. Bunch, M. Anselmino, Stroke-independent contribution of atrial fibrillation to dementia: a meta-analysis, Open Heart 6 (1) (2019) e000984.

[7] F. Gaita, L. Corsinovi, M. Anselmino, C. Raimondo, M. Pianelli, E. Toso, et al., Prevalence of silent cerebral ischemia in paroxysmal and persistent atrial fibrillation and correlation with cognitive function, J. Am. Coll. Cardiol. 62 (21) (2013) 1990–1997.

[8] D. Conen, N. Rodondi, A. Müller, J.H. Beer, P. Ammann, G. Moschovitis, et al., Relationships of overt and silent brain lesions with cognitive function in patients with atrial fibrillation, J. Am. Coll. Cardiol. 73 (9) (2019) 989–999.

[9] L. Rivard, P. Khairy, Mechanisms, clinical significance, and prevention of cognitive impairment in patients with atrial fibrillation, Can. J. Cardiol. 33 (12) (2017) 1556–1564.

[10] L. Rivard, L. Friberg, D. Conen, J.S. Healey, T. Berge, G. Boriani, et al., Atrial fibrillation and dementia: a report from the AF-SCREEN international collaboration, Circulation 145 (5) (2022) 392–409.

[11] M. Anselmino, S. Scarsoglio, L. Ridolfi, G.M. De Ferrari, A. Saglietto, Insights from computational modeling on the potential hemodynamic effects of sinus rhythm versus atrial fibrillation, Front. Cardiovasc. Med. 9 (2022) 844275.

[12] P. Calvert, D. Gupta, G.Y.H. Lip, The neurocognitive effects of atrial fibrillation: benefits of the ABC pathway, Eur. Heart J. Cardiovasc. Pharmacother. 9 (5) (2023) 413–420.

[13] M. Gardarsdottir, S. Sigurdsson, T. Aspelund, H. Rokita, L.J. Launer, V. Gudnason, et al., Atrial fibrillation is associated with decreased total cerebral blood flow and brain perfusion, Europace 20 (8) (2018) 1252–1258.

[14] M. Gardarsdottir, S. Sigurdsson, T. Aspelund, V.A. Gardarsdottir, L. Forsberg, V. Gudnason, et al., Improved brain perfusion after electrical cardioversion of atrial fibrillation, Europace 22 (4) (2020) 530–537.

[15] M. Anselmino, S. Scarsoglio, A. Saglietto, F. Gaita, L. Ridolfi, Transient cerebral hypoperfusion and hypertensive events during atrial fibrillation: a plausible mechanism for cognitive impairment, Sci. Rep. 6 (2016) 28635.

[16] S. Scarsoglio, A. Saglietto, M. Anselmino, F. Gaita, L. Ridolfi, Alteration of cerebrovascular haemodynamic patterns due to atrial fibrillation: an in silico investigation, J. R. Soc. Interface 14 (129) (2017) 20170180.

[17] A. Saglietto, S. Scarsoglio, L. Ridolfi, F. Gaita, M. Anselmino, Higher ventricular rate during atrial fibrillation relates to increased cerebral hypoperfusions and hypertensive events, Sci. Rep. 9 (1) (2019) 3779.

[18] A. Saglietto, S. Scarsoglio, L. Ridolfi, D. Canova, M. Anselmino, Cerebral spatially resolved near-infrared spectroscopy (SRS-NIRS): paving the way for non-invasive assessment of cerebral hemodynamics during atrial fibrillation, Minerva Cardiol.

Angiol. 69 (2) (2021) 124–126.
[19] A. Saglietto, S. Scarsoglio, D. Canova, S. Roatta, N. Gianotto, A. Piccotti, et al., Increased beat-to-beat variability of cerebral microcirculatory perfusion during atrial fibrillation: a near-infrared spectroscopy study, Europace 23 (8) (2021) 1219–1226.
[20] A. Saglietto, E. Bertello, M. Barra, I. Ferraro, C. Rovera, F. Orzan, et al., MRI pattern characterization of cerebral cardioembolic lesions following atrial fibrillation ablation, Front. Cardiovasc. Med. 11 (2024) 1327567.
[21] A. Deyranlou, J.H. Naish, C.A. Miller, A. Revell, A. Keshmiri, Numerical study of atrial fibrillation effects on flow distribution in aortic circulation, Ann. Biomed. Eng. 48 (4) (2020) 1291–1308.
[22] A. Deyranlou, C.A. Miller, A. Revell, A. Keshmiri, Effects of ageing on aortic circulation during atrial fibrillation; A numerical study on different aortic morphologies, Ann. Biomed. Eng. 49 (9) (2021) 2196–2213.
[23] A. Masci, L. Barone, L. Dedè, M. Fedele, C. Tomasi, A. Quarteroni, et al., The impact of left atrium appendage morphology on stroke risk assessment in atrial fibrillation: a computational fluid dynamics study, Front. Physiol. 9 (2019) 1938.
[24] G. Musotto, A. Monteleone, D. Vella, B. Zuccarello, R. Cannova, A. Cook, et al., Fluid-structure interaction analysis of the thromboembolic risk in the left atrial appendage under atrial fibrillation: effect of hemodynamics and morphological features, Comput. Meth. Prog. Bio. 246 (2024) 108056.
[25] F. Mori, F. Ishida, T. Natori, H. Miyazawa, H. Kameda, T. Harada, et al., Computational fluid dynamics analysis of lateral striate arteries in acute ischemic stroke using 7T high-resolution magnetic resonance angiography, J. Stroke Cerebrovasc. Dis. 28 (11) (2019) 104339.
[26] J. Liu, Z. Yan, Y. Pu, W.S. Shiu, J. Wu, R. Chen, et al., Functional assessment of cerebral artery stenosis: a pilot study based on computational fluid dynamics, J. Cereb. Blood Flow Metab. 37 (7) (2017) 2567–2576.
[27] S. Scarsoglio, A. Saglietto, F. Tripoli, J.J.M. Zwanenburg, G.J. Biessels, G.M. De Ferrari, et al., Cerebral hemodynamics during atrial fibrillation: computational fluid dynamics analysis of lenticulostriate arteries using 7 T high-resolution magnetic resonance imaging, Phys. Fluids 34 (12) (2022) 121909.
[28] A. Saglietto, S. Scarsoglio, F. Tripoli, J.J.M. Zwanenburg, G.J. Biessels, G.M. De Ferrari, et al., Atrial fibrillation hemodynamic effects on lenticulostriate arteries identified at 7-Tesla cerebral magnetic resonance imaging, Clin. Transl. Med. 13 (9) (2023) e1367.
[29] R.W. Regenhardt, A.S. Das, E.H. Lo, L.R. Caplan, Advances in understanding the pathophysiology of lacunar stroke: a review, JAMA Neurol. 75 (2018) 1273–1281.
[30] P.H. Stone, S. Saito, S. Takahashi, Y. Makita, S. Nakamura, T. Kawasaki, et al., Prediction of progression of coronary artery disease and clinical outcomes using vascular profiling of endothelial shear stress and arterial plaque characteristics: the PREDICTION Study, Circulation 126 (2012) 172–181.
[31] F. Gijsen, Y. Katagiri, P. Barlis, C. Bourantas, C. Collet, U. Coskun, et al., Expert recommendations on the assessment of wall shear stress in human coronary arteries: existing methodologies, technical considerations, and clinical applications, Eur. Heart J. 40 (2019) 3421–3433.
[32] L.R. Caplan, Lacunar infarction and small vessel disease: pathology and pathophysiology, J. Stroke 17 (2015) 2–6.
[33] A. Updegrove, N.M. Wilson, J. Merkow, H. Lan, A.L. Marsden, S.C. Shadden, SimVascular: an open source pipeline for cardiovascular simulation, Ann. Biomed. Eng. 45 (3) (2017) 525–541.
[34] H. Lan, A. Updegrove, N.M. Wilson, G.D. Maher, S.C. Shadden, A.L. Marsden, A re-engineered software interface and workflow for the opensource SimVascular cardiovascular modeling package, J. Biomech. Eng. 140 (2) (2018) 024501.
[35] W.H. Bouvy, G.J. Biessels, H.J. Kuijf, L.J. Kappelle, P.R. Luijten, J.J.M. Zwanenburg, Visualization of perivascular spaces and perforating arteries with 7T magnetic resonance imaging, Invest. Radiol. 49 (2014) 307–313.
[36] S. Scarsoglio, A. Guala, C. Camporeale, L. Ridolfi, Impact of atrial fibrillation on the cardiovascular system through a lumped-parameter approach, Med. Biol. Eng. Comput. 52 (2014) 905–920.
[37] M. Anselmino, S. Scarsoglio, A. Saglietto, F. Gaita, L. Ridolfi, A computational study on the relation between resting heart rate and atrial fibrillation hemodynamics under exercise, PLoS ONE 12 (1) (2017) e0169967.
[38] N. Westerhof, N. Stergiopulos, M.I.M. Noble, B.E. Westerhof, Snapshots of Hemodynamics, Springer, New York, 2005.
[39] M. Piccinelli, A. Veneziani, D.A. Steinman, A. Remuzzi, L. Antiga, A framework for geometric analysis of vascular structures: application to cerebral aneurysms, IEEE Trans. Med. Imaging 28 (2009) 1141–1155.
[40] L. Antiga, D.A. Steinman, Robust and objective decomposition and mapping of bifurcating vessels, IEEE Trans. Med. Imaging 23 (2004) 704–713.
[41] A.M. Malek, S.L. Alper, S. Izumo, Hemodynamic shear stress and its role in atherosclerosis, J. Am. Med. Assoc. 282 (21) (1999) 2035–2042.
[42] C. Cheng, D. Tempel, R. Van Haperen, A. Van Der Baan, F. Grosveld, M.J.A.P. Daemen, et al., Atherosclerotic lesion size and vulnerability are determined by patterns of fluid shear stress, Circulation 113 (23) (2006) 2744–2753.
[43] C. Hahn, M.A. Schwartz, Mechanotransduction in vascular physiology and atherogenesis, Nat. Rev. Mol. Cell Biol. 10 (1) (2009) 53–62.
[44] J.J. Chiu, S. Chien, Effects of disturbed flow on vascular endothelium: pathophysiological basis and clinical perspectives, Physiol. Rev. 91 (1) (2011) 327–387.
[45] V. Djulejić, S. Marinković, A. Maliković, I. Jovanović, D. Djordjević, M. Ćetković, et al., Morphometric analysis, region of supply and microanatomy of the lenticulostriate arteries and their clinical significance, J. Clin. Neurosci. 19 (10) (2012) 1416–1421.